M. Morelli, B.Y. Zhou, A. Guardone
Acoustic Characterization of Glaze and Rime Ice Structures on an Oscillating Airfoil via Fully Unsteady Simulations
Journal of the American Helicopter Society, Vol. 65, In press - Published online 18/06/2020
doi:10.4050/JAHS.65.042004

Acoustic Characterization of Glaze and Rime Ice Structures on an Oscillating Airfoil via Fully Unsteady Simulations

Myles Morelli*

PhD Candidate

Politecnico di Milano & University of Glasgow

Milan, Italy

Beckett Y. Zhou

Research Scientist

TU Kaiserslautern

Kaiserslautern, Germany

Alberto Guardone

Full Professor

Politecnico di Milano

Milan, Italy

Abstract

The development of low-cost and simple technologies to improve pilot awareness of icing environments is crucial to improve the safety of rotorcraft, and especially those with limited icing clearance which are admittedly operating within icing environments without full icing clearance. An acoustic characterization of glaze and rime ice structures is hereby introduced to begin to quantify different ice shape noise signatures which directly transcend from the iced performance characteristics in order

* Corresponding Author; email: mylescarlo.morelli@polimi.it

Presented at the Vertical Flight Society 75th Annual Forum & Technology Display, Philadelphia, Pennsylvania, May 13–16, 2019.

to develop acoustic ice detection technologies. The feasibility of the detection technique is assessed for fully unsteady simulations of ice accretion on an oscillating, two dimensional airfoil. This work focuses on the computational modelling of the experimental database of a rotor airfoil with pitching motion during icing conditions from the NASA Glenn Icing Research Wind Tunnel and computing the resultant noise signals and analyzing their topology.

Introduction

In-flight icing is a challenging problem for aviation authorities, manufacturers, operators, and pilots alike. Rotorcrafts restricted flight envelope means that the operators standard protocol to *"deviate from course to avoid and navigate around any encountered icing conditions"* (Ref. 1) and manufacturers flight manual instructions to *"prohibit flight in freezing rain or icing conditions"* (Ref. 2) is a frequently unobtainable idealized scenario. This makes operating rotorcraft in conditions where in-flight icing is foreseeable an inherently high-risk flight situation. In the US alone since as lately as 2016, there have been multiple in-flight rotorcraft icing accidents recorded, of which many which have included fatalities (Refs. 3–9). Through investigating these accidents it was found that 25% of the aircraft are completely destroyed on impact when exposed to dangerous levels of icing and that the accidents have an alarmingly high fatality rate of 71%.

The need to further understand the rotorcraft in-flight icing problem is clear, however, certification for flight in icing conditions is a demanding and expensive endeavour. If rotorcraft are to have certified Full Ice Protection Systems (FIPS) to allow them to operate in known icing conditions for full icing clearance they are required to oblige with Part 29-C of the regulatory code laid out by the European Aviation Safety Agency (EASA) and the Federal Aviation Authorities (FAA) (Refs. 10, 11). This requires rigorous testing for main and tail rotor blade anti-and de-icing protection systems, heated windscreens, and ice detection systems. Testing these ice protection systems for certification, however, is a non-trivial task. Data for certification can typically come from many sources including in-flight testing and experimental testing.

In-flight testing provides the ultimate source of data however it comes with a high cost and with large amounts of uncertainty as the ice shapes cannot be measured accurately during flight (Refs. 12–14). Fur-

thermore, flight testing requires specific meteorological conditions which cannot be controlled so the reproducibility of the test conditions and hence the ice shapes is problematic. Recent icing trails for the qualification of new aircraft have utilized the helicopter icing spray system (HISS) to help control icing conditions such as the intensive test campaign of AugstaWestland's AW101 demonstrator aircraft "CIV01" in January of 2009 (Ref. 15). Stationary test rigs such as the Canadian National Research Council spray rig have also been introduced to further improve control over icing parameters during in-flight testing, however, they are limited to hover flight conditions (Ref. 16). Experimental tests in icing wind tunnels provide the most control over icing conditions yet the need to use model rotors introduces additional ice scaling parameters (Refs. 17, 18). Discrepancies between model and full-scale rotor ice shapes have been documented even with the use of ice scaling parameters leading to further research dealing with this issue (Ref. 19).

The use of computational modeling to simulate ice shapes on rotor blades helps further understand the rotorcraft icing problem (Refs. 20, 21). As with so many other aerospace technologies, rotorcraft icing codes lag behind fixed-wing aircraft icing codes which have been well established for many years now. This is partly due to the additional complexities that the rotor blade introduces which results in a highly unsteady flow field. Subsequently, icing on the main rotor blade of a helicopter should be considered inherently as an unsteady problem which makes simulating the process challenging. Hence, rotorcraft icing simulations are required to include both the effect of the centrifugal force and the effect of the blade oscillations on the final ice shape. This however requires the use of high-fidelity icing codes which is computationally challenging.

A joint venture in 2010 between Bell Helicopter, The Boeing Company, Sikorsky Aircraft, Georgia Institute of Technology, and NASA set out to enhance understanding of rotorcraft icing with the development and validation of high-fidelity icing analysis tools. With the consensus that current data was insufficient for validation two main experimental initiatives were outlined: 1). A high-quality oscillating airfoil test to enhance the scarce dataset for validating the rotorcraft icing problem during pitching motion (Ref. 22) and 2). A spinning rotor test to assess the feasibility of ice scaling parameters and evaluate hydrophobic and icephobic materials (Ref. 23). These experimental tests were then the basis for the validation of high-fidelity computational rotorcraft icing tools (Refs. 24, 25). This work focuses on the

validation of the oscillating airfoil test and uses the experimental test data from Reinert et al. (Ref. 22) and calculated ice shapes from Narducci and Reinert (Ref. 25) for ice shape comparisons.

As part of this collaboration between the US Government and industry, The Boeing Company calculated ice shapes on an oscillating airfoil (Ref. 25) and used the experimental work conducted in the NASA Glenn Icing Research Tunnel (IRT) (Ref. 22) to validate the code. The main goal of the work was to accurately calculate oscillating airfoil ice shapes and resultant performance characteristics. The analysis approach used was built on the premise that the ice shape is not a strong function of the frequency of oscillation which was supported by the similarity in ice shapes with different oscillatory frequencies. A further assumption was then made that the time history of a helicopter rotor blade pitching at 1/rev can be represented by a very slow-moving blade. Accordingly, it was then assumed that only the mean angle of attack and extreme amplitudes of angle of attack are considered in a series of quasi-static icing events.

One of the main drawbacks of this method, however, is that it does not consider the effect of the unsteady flow field as the ice accretes. To help theoretically understand if a flow field can be considered as steady the reduced frequency is regularly used. The degree of unsteadiness of the oscillation can be expressed by the reduced frequency and defined in terms of the semi-chord, $b = c/2$. Where the factor of $c/2$ is inserted so that the reduced frequency becomes dimensionally correct (Ref. 26). The reduced frequency, k and then be given as,

$$\text{Reduced Frequency, } \; k = \frac{\omega c}{2V_\infty} \tag{1}$$

for $0 \leq k \leq 0.05$ flow can be considered quasi-steady and for $k \geq 0.05$ flow is considered unsteady (Ref. 27), where ω is the oscillatory frequency and V_∞ is the free stream velocity. For a rotor blade pitching 1/rev this may in certain cases be applicable, however, this is not positive for all instances.

Alternative approaches to predict ice shapes were also suggested in Ref. 25 which merit discussion. The first alternative approach suggested was an average angle of attack, however, then the airfoil does not oscillate and the simulation is considered entirely steady. The second alternative approach proposed was an averaging of ice shapes, where, a clean airfoil is iced at various static angles of attack and using weighted averages the final ice shape is computed. This also considers the unsteady oscillating airfoil to

be steady and again neglects all aerodynamic characteristics and hysteresis behaviour associated with the oscillating motion of the airfoil outlined in Ref. 25.

Five years later in 2015 another collaboration arose between The Boeing Company, Georgia Institute of Technology, Penn State University, and NASA, which involved much of the same personnel, and aimed to further develop and progress rotorcraft icing computational tools (Ref. 28). This study focused on coupled CFD/CSD analysis for rotorcraft in forward flight to assess the trim state of an iced rotor. Once again however this used the method to assume that the time history of an oscillating airfoil can be represented by a slow-moving blade so that eventually the icing analysis can be thought of as a series of quasi-static events.

Since as recently as 2016, experimental work from Cheng et al. begun to help develop technologies to detect ice formation through the quantification of rotor surface roughness due to ice via broadband noise measurements (Ref. 29). Several tests were conducted at different roughness levels to measure the broadband noise during the early stages of ice accretion. Two parameters, the arithmetic average roughness height, and, the average roughness height based on the integrated ice thickness at the blade tip were used to describe the ice-induced roughness. The study found that the high-frequency spectra of the rotor broadband noise was particularly sensitive to the blade surface roughness.

An alternative approach later proposed by Chen et al. (Ref. 30) in 2018 involved numerical simulations of ice accretion and computing the far-field noise signature of the iced rotor blade shape using computational aeroacoustics. This work used a very small prescribed ice notch at various ice lengths along the rotor and measured its influence on the acoustics of different rotor blade sets in hover and forward flight. It found that for limited lengths of ice accretion, the location of the sound monitor is important to successfully capture any difference in the acoustic characteristics of iced rotors.

The goal of this work is to establish the first acoustic characterization of glaze and rime ice structures to aid in further developing acoustic ice detection warning systems for improving rotorcraft flight safety. The NASA Glenn IRT database of a pitching rotor airfoil during icing conditions has been identified as it produces a vast array of ice structures. The test cases chosen from this experimental database are first described within the paper. The unsteady computational methods used for simulating the ice shapes are then introduced alongside a spatial convergence study. The computational results of the different test cases are

then discussed. Each of the test cases then analyzes the ice structure, the performance degradation due to the ice formation, the iced airfoil flow field, and the iced airfoil acoustics. The objective is thus to categorize the sound spectra of the glaze and rime ice structures and link the acoustics signals to the known performance characteristics of glaze and rime ice structures to further improve rotorcraft safety. With this concept being in the early stages of development, there are many limitations of this work through the simplification of only considering a pitching rotor airfoil, however despite this, much of this work serves as a proof-of-concept for further developments in the near future. These limitations mainly revolve around the simulations being considered as two-dimensional, meaning no centrifugal forces are considered during in the ice formation, and, the computational aeroacoustics does not account for important three-dimensional noise sources such as impulsive blade vortex interactions. The turbulent flow separating from the leading edge of an iced rotor blade is typically also three-dimensional in nature, and whilst only considering a two-dimensional airfoil, this remains another limitation to the study.

Experimental Test Cases

The computations of the oscillating airfoil ice shapes are compared against both experimental work and other computational in-flight icing codes. Thanks to the experimental icing tests which took place in the NASA Glenn IRT to help improve the scarce data-set of oscillating airfoils numerous different test cases have been identified. The experimental work from Rienert et al. (Ref. 22) has been used for verification of the icing computations within this work. The icing computations from Narducci and Rienert are then shown for code comparisons using their IceMaker software (Ref. 25). At the time of the experiment, acoustic noise signals were not being considered within the consortium for the use as ice detection systems. For this reason, there was no acoustic data recorded of the oscillating airfoil ice shapes.

These test cases assess the effect of the flow field on the ice shapes, the meteorological conditions which are inherently the driver causing icing, and the length of time when exposed to icing conditions. The operating conditions from these test cases used for examination can be found in Table 1.

The different operating conditions represent an airfoil at both low and high flight speeds and at both low and high mean angles of attack with significant amplitudes of oscillations. The length of time exposed

to icing conditions is long enough to expect significant ice accretion such that it could have severely damaging effects on the performance of the airfoil. The Mean Volume Diameter (MVD) of the supercooled water droplets within these cases is constant at $22\ \mu m$ and is of a typical value for many icing experiments. The liquid water content (LWC) of the supercooled water droplets ranges from moderate to high. Two different oscillating frequencies were discussed at which a conventional helicopter rotor blade would pitch per revolution, one a high-frequency oscillation at 5.6 Hz and the other a low-frequency oscillation at 2.8Hz. Results showed that the effect of the rate of oscillation was minimal on the final ice shape and as there was more experimental data openly available for the icing tests with the lower frequency of oscillation, simulations were conducted with an oscillation rate of 2.8Hz. The effect of the rate of oscillation on the ice shapes is, however, a parameter that will be considered at a later date. One of the most intriguing conditions from the experimental tests is the outside air temperature (OAT) which is at $-14\ ^{\circ}C$. The OAT is representative classically of mixed rime-glaze ice accretion which can during extensive ice formation lead to the formation of symmetrical double-horn structures. These ice structures are renowned for being demanding to simulate and require an accurate ice accretion model to account for the heat diffusion within the ice layer and mass transfer from glaze to rime ice cells.

The experimental tests consisted of an untwisted Sikorsky SC2110 wing designed by Sikorsky/Lednicer and Owen as a rotorcraft airfoil and is undergoing pitch oscillation. The wing dimension has a 0.381m chord and stretches from the floor to the ceiling of the wind tunnel. The airfoil has a maximum thickness at 9.9% at 37.7% chord and has a maximum chamber of 1.9% at 15.7% chord. Work from Zocca et.al has shown that the interference of wind tunnel walls in the NASA Glenn IRT does not greatly influence the final ice shape at the central station of the airfoil and so icing simulations can essentially be considered two-dimensional (Ref. 31). This, however, was tested based on a steady icing wind tunnel experiment and did not look further into three-dimensional effects introduced from unsteady flow fields. For simplicity and to ensure this analysis is within the scope of the timeline of the project the impending icing simulations are considered to be two-dimensional. This is also in agreement with the results obtained from the oscillating airfoil ice shapes which report little change along the spanwise direction although this is something that will require further investigation.

Computational Method

The open-source SU2 software suite was used to determine the unsteady flow field over the oscillating airfoil (Ref. 32). The SU2 software suite solves partial differential equations on general unstructured grids. The core of the suite is a Reynolds-averaged Navier-Stokes (RANS) solver which was used in this simulation in tandem with the Menter shear-stress transport turbulence model. Spatial discretization was achieved using an edge-based finite volume method. The convective and viscous fluxes are then evaluated at the midpoint of an edge. The Jameson-Schmidt-Turkel numerical scheme was used to solve the convective fluxes with a 2^{nd} order limiter for the up-wind convective scheme. Whilst to evaluate the viscous fluxes using a finite volume method the Green-Guass numerical scheme was used. To account for the unsteady nature of the problem a 2^{nd} order accurate dual-time-stepping approach was used to transform the unsteady problem into a series of steady problems. Each physical time-step was then solved consecutively for a fictitious time until converged to a steady-state problem. A volumetric rigid motion was used to account for the sinusoidal movement of the oscillating airfoil where the whole grid rotates about a centred origin at each physical time-step. Convergence acceleration was achieved using an agglomeration multi-grid implementation to generate 4-levels of grid coarsening from the provided fine grid at run-time.

In-house codes PoliDrop and PoliMIce were used to respectively to determine the collection efficiency and final ice shapes (Ref. 33). The PoliDrop code is a Lagrangian based particle tracking code which uses previously computed flow field data to determine the particle trajectories and impingement locations. The code has been developed to account for moving boundaries present in unsteady problems. After computing the particle trajectories it calculates the value of the collection efficiency, β which can be thought of as the collected mass of particles on the impacted area divided by the mass of the total number of particles in the entire cloud and is given by

$$\beta = \frac{V_t}{V_c} \frac{\sum N_i}{\sum D_i} \tag{2}$$

where N_n is the number of impacted by particles, D_n is the total number of droplets, and $V_{c,\,t}$ is the volume of the impacted cloud and total cloud respectively.

The PoliMIce software library provides state-of-the-art ice formation models. The model used in this

work to capture the complex experimental ice shapes is the local exact solution of the unsteady Stefan problem for the temperature profiles within the ice layer in glaze conditions (Ref. 34). This model moves from Myers' formulation and includes an unsteady description of the heat diffusion problem within the ice layer and uses local values of the air temperature outside the boundary layer to compute the convective heat fluxes. Furthermore, it is able to account for the mass transfer between rime and glaze regions. The ice shapes are then computed using an unsteady multi-step approach, whereby, non-linear ice accretion is accounted for by iteratively updating the surface solution on which the ice accretes.

Within this research ice accretion on an oscillating airfoil is considered inherently as a fully unsteady problem to aid in further developing rotorcraft icing tools. It thus accounts for the iced airfoil geometry, reduced frequency, and amplitude of oscillations which are the primary factors causing dynamic stall (Ref. 35). This is achieved using the process shown in Fig. 1 where the collection efficiency on the airfoil over a full period of oscillation is calculated. In doing so the impingement limits and distribution of super-cooled water droplets fully take into account any possible unsteady aerodynamic flow field effects. This is ensured so that at every unsteady aerodynamic pseudo-time at which the airfoil oscillates, there is a cloud front of super-cooled water droplets impacting on the airfoil. The collection efficiency is then calculated after a full oscillation of the airfoil once it passes through the cloud. This information is then passed onto the icing solver PoliMIce which, using ice accretion laws governed by the meteorological conditions during flight, computes the newly formed ice shape. This process is then iteratively solved in a multi-step process for a given length of ice accretion. In this approach there is no assumption of steady or quasi-steady flow even whilst $0 \leq k \leq 0.05$.

The clean and iced airfoil shapes are then subject to a computational aeroacoustic (CAA) analysis using the permeable-surface Ffowcs-Williams-Hawkings (FWH) formulation in SU2 (Ref. 36), in order to help predict the early stages on ice accretion during flight to aid in warning the pilot of ice formation. The permeable FWH formulation allows fluid to flow through the fictitious surface Γ_p. Details of the flow field are then extracted and the noise source is then propagated to the far-field. This implementation is shown in the schematic from Figure 2. The computational domain is thus divided into two separate regions; the near-field CFD region, Ω_1 and the far-field CAA region, Ω_2. The permeable surface Γ_p can be described by the shape function, $\mathrm{f} = 0$ where if $\mathrm{f} < 0$ it is inside the surface and if $\mathrm{f} > 0$ it is outside the

surface. The position of the FWH lies $\frac{3}{4}$ chords length from the airfoil trailing edge. The position of the observer locations was chosen based on where noise would likely be perceived on a conventional main rotor/tail rotor helicopter, either under the main rotor directly or slightly forward or aft of it. Hence three different observer locations are used to assess the noise in the far-field at 10 chords length from the centre of the airfoil at $45°,\ 90°\ \&\ 135°$ from the inflow direction.

In accordance with the icing simulation, the acoustic analysis is likewise considered as a two-dimensional model, although it is understood the rotor blade noise is most definitely not two-dimensional in nature. Furthermore, the current unsteady Reynolds-averaged Navier-Stokes (URANS)-FWH approach does not account for non-uniform flow around the airfoil. If acoustic waveforms are subject to significant distortion, for instance during more representative test cases such as blade vortex interactions, this approach has its limitations. It is for this reason, that this analysis is just for a proof-of-concept for the detection of different ice structure characterizations.

Spatial Grid Convergence

The surface node spacing of the mesh was determined through examining the spatial convergence of the coefficient of lift, C_l and the coefficient of drag, C_d. With the shape of the ice formation and thus the mesh structure unknown before the computation, the study was conducted on an un-iced airfoil. A constant angle of attack of $\alpha = 5°$ was used opposed to a sinusoidal oscillating motion so direct comparisons of C_l and C_d could be examined that would be time-independent. Three levels of mesh refinement were assessed at a ratio of $r = 2$. Whilst the surface node spacing was being reduced at each mesh refinement level, the wall distance remained constant to ensure a near-wall $y^+ \leq= 1$. The results of the mesh refinement on the C_l and C_d are shown in Table 2.

The Richardson extrapolation method (Ref. 37) was used for obtaining higher-order estimates of the continuum value at zero grid spacing, f_{exact} from a series of lower-order discrete values $(f_1,\ f_2,\ ..,\ f_n)$. The objective values used here were the C_l and C_d and as the grid spacing reduces they approach an asymptotic zero-grid spacing value which is assumed to be close to the true numerical solution.

The order of convergence, p can be obtained from three solutions using a constant grid refinement

ratio, r and can be given as,

$$p = \ln\left(\frac{f_3 - f_2}{f_2 - f_1}\right) / \ \ln(r) \tag{3}$$

where the theoretical order of convergence is $p = 2$, however, this is not usually achievable due to the grid quality. The Richardson extrapolation can then be generalized by introducing the p^{th}-order methods to solve for f_{exact} and to estimate the continuum value,

$$f_{exact} \cong f_1 + \frac{f_1 - f_2}{r^p - 1} \tag{4}$$

whilst the relative error, ε can be described as,

$$\varepsilon_{i+1,i} = \frac{f_{i+1} - f_i}{f_i} \tag{5}$$

The grid refinement error estimator derived from the theory of the generalized form of the Richardson extrapolation was then used to determine the Grid Convergence Index, GCI (Ref. 38). The GCI provides a measure of the percentage the computed value is away from the value of the asymptotic numerical value. The GCI and can be written as,

$$GCI_{i+1,i} = F_S \frac{|\varepsilon_{i+1,i}|}{r^p - 1} \tag{6}$$

where a factor of safety, $F_S = 1.25$ was used. The results of the spatial convergence analysis are shown in Table 3. There is a reduction in the GCI value for successive grid refinements for both the C_l and the C_d. It shows that during the first mesh refinement, from level $1 \rightarrow 2$, there is a significant difference compared to the asymptotic numerical solution, f_{exact}. During the second mesh refinement however, from level $2 \rightarrow 3$, the difference from the asymptotic numerical solution, f_{exact} is less.

With there being minimal difference between the $2 \rightarrow 3$ mesh refinements, and with the extra computational cost undesirable, the 2^{nd} mesh refinement level was considered suitable and used for the subsequent computations. Thus, the mesh contained a node spacing at the surface of the airfoil of 0.0005 m. The mesh then contained a cluster of finer cells close to the leading and trailing edges. The far-field was placed 14

chord lengths from the airfoil with a spacing of 0.05 m. The overall size of the mesh was $42,614$ elements. A schematic of a close-up of the mesh around the clean airfoil is shown in Figure 3.

Numerical Results and Discussion

The results of the unsteady icing simulations from each of the different test cases are shown in Fig.4. Each of which displays the results from the NASA Glenn IRT experimental tests, the Boeing Company's "IceMaker" computational icing analysis tool-set, and the computations using the "PoliMIce" ice accretion software suite. All the performance characteristics and acoustic signals of these test cases have been simulated, nevertheless, for readability this paper only focuses on the effect of the glaze and rime ice shapes produced from conditions R-T600 and G-LWC shown in Table 1. These two exemplary test cases were chosen due to the LWC being the only influencing parameter on the ice structure allowing for a direct comparison of the performance characteristics and acoustic signals. The prediction of the lift and moment performance degradation caused from these two ice shapes is compared against the performance characteristics of a clean airfoil operating in the same flow conditions and is shown in Fig. 5. In each performance analysis, there is initially an assessment of the lift coefficient hysteresis loops. This is then proceeded by an assessment of the moment coefficient hysteresis loops. The performance characteristics can be further explained when examining the flow fields of the iced airfoils as depicted in Fig. 6. This is visualized through displaying the normalized velocity with spatially uniform streamlines at the minimum, mean and maximum angles of attack. The velocity magnitude is normalized by the incoming freestream velocity. The acoustic signals of clean and iced airfoils are then shown in Fig. 7. The acoustic pressure, $p' = p_{\text{observer}} - p_{\text{mean}}$ which can be defined as the fluctuating part of the far-field pressure around its mean, is normalized by the freestream pressure for each of the test cases. The normalized acoustic pressure is then shown at different observer locations from the centre of the oscillating airfoil. The noise signals are shown over a time window long enough to display the noise sources periodicity. At all observer locations, the rate of oscillation drives the harmonic frequency of the pressure perturbations. The magnitude of the acoustic pressure in all cases is significant to be detectable. The continuous noise signals are then described in terms of how the power of the signal is distributed over frequency using a power spectral

density diagram to characterize the noise signals produced from the glaze and rime ice structures and is shown in Fig. 8.

Icing Analysis

The first test case considered is condition R-T600 from the experimental work shown in Table 1. This is considered to be the baseline test condition which all other flow fields and meteorological conditions are based on for the comparison of ice shapes. R-T600 is a low flight speed case with a moderate value of LWC present during icing conditions. The results of the icing simulation of R-T600 are shown in Fig. 4a. The simulated ice shapes produced from PoliMIce display a characteristic "spearhead" generated typically during rime ice conditions. The ice thickness appears moderate with slight asymmetry caused by the mean angle of attack. The experimental results show a rougher shape than the results computed from PoliMIce. The rough feather shapes were found to be very difficult to capture due to their large irregularities over the surface. The overall shape however appears to be in very good agreement with the experimental data. In particular agreement is the impingement limits of ice on the upper and lower surface of the airfoil. The IceMaker code from Boeing is used for code comparison with their quasi-static icing approach (Ref. 25). The results from PoliMIce using the fully unsteady collection efficiency approach share many similarities with the results from IceMaker. Both codes, however are unable to replicate the uneven ice profile and approximate smoothed curves opposed to the much rougher experimental ice shape. This however is not of the greatest concern as the reproducibility of these experimental uneven shapes would likely change from one experimental test to another.

The second test case considered is condition G-LWC from the experimental database displayed in Table 1. This test case is identical to R-T600 except for a single environmental condition, the LWC. In this case, there is a higher value of LWC at the upper scope of which would be expected in the meteorological environment. This means that the initial clean airfoil experiences the same flow conditions in both test cases and differences only arise after the first step of the multi-step ice accretion. Therefore, every droplet of super-cooled water impacting on the airfoil contains a greater quantity of liquid water per cubic meter, resulting in, greater rates of ice accretion. The results of the icing simulation from condition G-LWC

are shown in Fig. 4b and produce distinct "double-horn" ice structures paradigmatic of mixed glaze-rime ice regimes. This is by far the most challenging of shapes simulated as it demands an ice accretion model which has an accurate account of the local air temperature and the mass flux of liquid water from neighbouring cells. At the stagnation point, the static air temperature is higher producing a large amount of liquid water and as it runs back it reaches areas of lower air temperature giving rise to the double-horn ice structure. The reason behind the double-horn ice structure being present here and not in R-T600 is due to there being less LWC per super-cooled water droplet meaning there is less mass flux of liquid water between neighbouring cells and a lower rate of ice accretion. The ice shape results themselves are in good correlation with the experimental data especially the upper horn which is very closely reassembled. The lower horn is offset slightly, however, despite this, the general shape is within good proximity to the experimental data. Similarly to the previous test case the computed ice shapes fail to capture the roughness of the ice.

The third test case considered is condition R-T900 from the experimental work shown in Table 1. This test case is identical to condition R-T600 except for the period of which the airfoil is exposed to the icing environment. This test case extends the duration of time exposed to the icing environment from 600 seconds to 900 seconds. This test case also reverts to more moderate values of liquid water content contained within the super-cooled water droplets. The results of the icing simulation associated to condition R-T900 are shown in Fig. 4c. The simulated ice shape displays an extension of the characteristic "spearhead" displayed previously from condition R-T600 in Fig.4a. The analogy can thus be confirmed that the ice thickness is indeed a function of icing time as one would expect. Unsurprisingly then, since the flight conditions and the meteorological environment remain the same and with only the duration of icing time influencing the ice shape, the thickness of ice is the only parameter affected.

The penultimate test case considered is condition G-AoA5 outlined in Table 1. This is regarded as the high-speed test case where the incoming flow is at Mach 0.4. All other test conditions remain the same as in the baseline test. The increase in freestream velocity has the effect that it increases the kinetic energy of the airfoil and subsequently reverberates in an increase in the airfoil surface temperature. Fundamentally, the outcome of this means the ice regime moves away from the dominantly rime conditions and towards mixed glaze-rime conditions, thus different ice structures are present. The formation of double-horn ice

structures can hence be observed in Fig. 4d. This double-horn ice feature appears to be well represented again by the PoliMIce icing software when compared against the experimental results.

The final test case considered is condition G-AoA10 based on the experimental research and its details are shown in Table 1. This is another high-speed test case where the incoming flow is at Mach 0.4. The influential parameter assessed here is the mean angle of attack. This airfoil is operating at higher angles of attack with a mean amplitude of $10 \pm 6°$. As this is a high-speed case double-horn ice structures are present once more as observed in Fig. 4e. The increase in the mean angle of attack, however, exacerbates the asymmetry of the ice structure. This intensifies the upper-horn ice structure making it more prolific than the lower-horn ice structure which is subsequently weakened. The upper-horn ice structure was predicted markedly close to the experimental work, however, the lower-horn ice structure was found to be difficult to predict.

Performance Analysis - Glaze vs Rime

The lift coefficient produced from the rime ice structure of condition R-T600 is shown in Fig. 5a. Immediately it is noticed how close the two lift hysteresis loop results correlate and in fact, the iced airfoil increases the lift coefficient. This result can be explained by the fact that as the ice thickness increases the characteristic length used to compute the lift coefficient remains unchanged giving rise to an increase in lift. Furthermore, the smooth ice shape does not greatly disturb the airfoils flow characteristics. It also effectively increases the airfoil chamber which may slightly help at high angles of attack during low flight speeds.

The moment coefficient produced from the rime ice structure of condition R-T600 is shown in Fig. 5b. It is clear here that despite the lift coefficient remaining largely unaffected by the ice structure, the moment coefficient is affected quite severely by icing even with such aerodynamically acceptable ice shapes. At low angles of attack, there is a stronger nose-up pitching moment and at high angles of attack, there is a stronger nose-down pitching moment when in comparison with the clean airfoil moment characteristics. The thickness of the hysteresis loop also broadens compared to the thickens of the clean airfoil. Despite this, the moment coefficient hysteresis loops share the same profiles. These differences may be attributed

to the ice increasing the chord and changing the location of the $\frac{1}{4}$chord at which the moment is computed. Although the increase in chord due to ice is slight it is clear that is has a significant effect on the moment coefficient computations.

The lift coefficient produced from the glaze ice structure of condition G-LWC is shown in Fig. 5c. Unlike the previous test case, the difference between the results is clear-cut and the lift coefficient hysteresis loops show little similarity. The iced airfoil depicts an airfoil experiencing dynamic stall as it approaches high angles of attack. On the upstroke of the oscillation, the lift coefficient is consistently less and as the airfoil reaches around 9° it experiences stall leading to a large reduction in lift. On the down-stroke, after the period of stall, the lift coefficient settles as the flow reattaches and the lift coefficient reduces with the angle of attack. Here the increase in chord length appears insignificant compared the shape of the ice structure to increase the lift coefficient.

The moment coefficient produced from the glaze ice shape of condition G-LWC is shown in Fig. 5d. Immediately it is apparent the detrimental effect the ice shape has on the moment coefficient and in particular dynamic stall. On the upstroke of the oscillation, the moment coefficient fluctuates at a slight order of magnitude lower than the clean airfoil. As the airfoil reaches around 9° stall occurs and there is a severe peak in the moment coefficient causing a strong nose-up moment. On the down-stroke of the oscillation, as the flow becomes reattached to the surface, the moment coefficient settles and again begins to fluctuate at a lower order of magnitude.

Flow-field Analysis - Glaze vs Rime

The results from Fig. 6a show that the rime ice shape from Fig. 4a has very minimal effect on the flow field. As the flow passes over the leading edge of the iced airfoil it remains attached to the upper surface at all angles of attack. The stagnation location is not affected and there is no flow separation from this ice shape. It is for this reason why the two observed performance characteristics of the clean and iced airfoils remain largely recognizable as shown in Fig. 5a & 5b.

The results from Fig. 6b show the severity the glaze double-horn ice structure displayed in Fig. 4b has on the flow field as it induces large amounts of flow separation causing dynamic stall. A stagnation point is

present at the centre location of the two horns and as the flow moves downstream it is shown to accelerate around the horns. At the minimum angle of attack, its shows that aft of the lower horn there is a strong vortex produced generating an area of chaotic flow. As the airfoils angle of attack increases the strength of the vortex aft of the lower horn decreases and the strength of the vortex aft of the upper horn increases. When the airfoil reaches the maximum angle of attack it shows complete flow separation from the airfoils upper surface causing the dynamic stall shown in the lift coefficient in Fig. 5c. The fluctuations in the moment coefficient in Fig. 5d may be explained by the strengthening and weakening of the two vortices just aft of the upper and lower horns until high angles of attack when the large scale vortex on the upper surface dominates causing dynamic stall.

Acoustic Analysis - Glaze vs Rime

The time history of the pressure perturbations producing the noise signals of the clean and rime iced airfoils from R-T600 are shown in Figure 7a. At all observer locations there is a very slight increase in fluctuations in normalized acoustic pressure of the rime iced airfoil at the peaks of the waves and as the strength of the signal increases the difference in normalized acoustic pressure increases with it as shown at observer location B. Due to there being such similar flow characteristics between the clean and iced airfoils as shown in Figure 6a the noise signals are almost identical.

The time history of the pressure perturbations producing the noise signals of the clean and glaze iced airfoils from G-LWC are shown in Figure 7b. The fluctuations in normalized acoustic pressure of the glaze iced airfoil, in this case, show vastly different noise signals than to the clean airfoil. Once again the frequency of the oscillating airfoil drives the pressure fluctuations so there is clear periodicity present. The visibly different noise signals are attributed to be caused by the significant differences in the flow field as shown in Fig. 6b. On the upstroke of the iced airfoil, the perturbations of normalized acoustic pressure show similar values to the clean airfoil. That is until the occurrence of the dynamic stall behaviour at which point large scale vortices are produced developing peaks of broadband noise at a magnitude far greater than the peaks of the clean airfoil noise signal. These peaks then begin to oscillate at a far higher frequency. Furthermore, what is noteworthy is the similarity between the high-frequency oscillations over

each main oscillation.

Acoustic Characterization of Glaze and Rime Ice Structures

The noise signals of all test cases are then described in terms of how the power of the signal is distributed over frequency through a power spectral density diagram shown in Fig. 8. Through analysing these signals it is clear that there is a distinct division between the high-frequency noise of the glaze and rime ice structures. The rime ice structures from conditions R-T600 and R-T900 display a tonal peak at 2.8 Hz corresponding to the oscillating frequency of the airfoil. The glaze ice structure from condition G-LWC displays identical noise level at this frequency. The glaze ice structures from conditions G-AoA5 and G-AoA10 exhibit an increase in the tonal noise at 2.8 Hz due to the increase in free-stream velocity. All glaze ice structures from conditions G-LWC, G-AoA5 and G-AoA10 then contribute to significant levels of noise at the higher frequency range of the sound spectra whilst there is minimal contribution from the rime ice structures.

Conclusion

An unsteady multi-step ice accretion method coupled with a fully unsteady collection efficiency approach is used here oversee the feasibility of predicting ice shapes over an airfoil oscillating in an unsteady flow field. Experiments from the NASA Glenn IRT were used for comparisons of ice shapes. The aerodynamics of the airfoil is modelled using an unsteady time accurate approach. The super-cooled water droplets are transported within the unsteady flow field and the airfoils moving boundaries are supported within the Lagrangian based particle tracking. The local solution of the unsteady Stefan problem was used to capture the complex experimental ice shapes. Ice shapes are then subject to a computational aeroacoustic analysis using the permeable-surface Ffowcs-Williams-Hawkings formulation. The acoustic signals produced from the varying ice structures can then be characterized into two distinct categories; glaze ice noise signals and rime ice noise signals. Overall some conclusions from this work can be drawn as follows:

1) The fully unsteady collection efficiency approach used to ensure unsteady aerodynamic effects are

imposed on the super-cooled water droplet trajectories helps predict ice shapes very close to the experimental data and especially for mixed rime-glaze ice double-horn ice structures.

2) The contrast in the effect the ice structure has on the performance characteristics is observed, and mixed rime-glaze ice double-horn ice structure displays severe degradation in performance and the occurrence of premature on-set stall.

3) The acoustic analysis shows definite scope for the use of computational aeroacoustics to help detect and characterize different types of ice formation in real-time for ice detection warning systems as the different glaze and rime ice structures produce recognizably different noise signatures.

It is apparent from this work that if a relatively simple and low-cost noise ice detection system was in place it would be possible to detect which type of ice accretion was present on the surface in real-time and the pilot would be able to react accordingly. This could be done by detecting large differences in the peak magnitude of the noise source or by detecting high-frequency noise sources associated to flow separation from double-horn ice structures.

With the inherent nature of rotor blades being largely dominated by three-dimensional flows the limitations of this work are understood, however, the fundamental principals behind this study will remain intact for the future when this work is to be extended to three-dimensional simulations of the full rotor. One area of particular interest, is the possibility of the use of scale resolving methods like the Delayed Detached Eddy Simulations (DDES) in SU2 (Refs. 40,41), to improve the resolution of the smaller scales and thus higher frequency noise signals caused from the double horn ice structures at the leading edge of the airfoil. A natural transition from the current work would be the acoustic characterization of glaze and rime ice structures on a pitching wing where three-dimensional effects are present at the wing tips. Another intriguing phenomena which would be present, is the formation of omega-type vortical structures, which are a generic feature of three-dimensional finite high aspect-ratio wings experiencing dynamic stall, and thus, as shown in the two-dimensional simulations within this work could have a significant impact on the acoustic signals during in-flight icing.

Author contact:

Myles Morelli – Email address: mylescarlo.morelli@polimi.it

Acknowledgements

This project has received funding from the European Union's H2020 research and innovation programme under the Marie Skłodowska-Curie grant agreement No 721920. Further information can be found at the Network for Innovative Training on ROtorcraft Safety (NITROS) project website.

References

[1]TEMSCO, "Air Ambulance Helicopter Operational Procedures," Temsco Helicopters Inc. Chapter IX, Revision 4, July 1997.

[2]EASA, "Type Certificate Data Sheet: Airbus Helicopters," AS 350/EC 130," EASA TCDS No. EASA.R.008, March 2018.

[3]Plagens, H. D, "National Transportation Safety Board Aviation Accident Final Report," NTSB No. WPR17FA047, December 2017.

[4]Cawthra, J., "National Transportation Safety Board Aviation Accident Final Report," NTSB No. WPR16LA104, June 2018.

[5]Hodges, M. J., "National Transportation Safety Board Aviation Accident Final Report," NTSB No. ANC16FA023, January 2018.

[6]Read, L. D., "National Transportation Safety Board Aviation Accident Final Report," NTSB No. ERA16LA167, October 2017.

[7]Cox, P. R., "National Transportation Safety Board Aviation Accident Final Report," NTSB No. ERA15FA096, January 2017.

[8]McKenny, V., "National Transportation Safety Board Aviation Accident Final Report," NTSB No. WPR15FA072, October 2016.

[9]Diaz, A. N., "National Transportation Safety Board Aviation Accident Final Report," NTSB No. ERA15FA085, March 2017.

[10]EASA, "Easy Access Rules for Large Rotorcraft (CS-29)," EASA Amendment 4, June 2018.

[11]FAA, "Certification of Transport Category Rotorcraft," Adivisory Circular No: 29-2C, May 2014.

[12]Belte, D., Ranaudo, R., "Initial Results from the Joint NASA-LEWIS/U.S. Army Icing Flight Research Tests," Proceedings of the 45th Annual Forum of the American Helicopter Society, Boston, Massachusetts, May 1989.

[13]Belte, D. and Woratschek, R., "Helicopter Icing Spray System (HISS) Evaluation and Improvement," U.S. Army Aviation Engineering Flight Activity, Project No.82-05-3, Edwards Air Force Base, California, April 1986.

[14]Peterson, A., Jenks, M., and Gaitskill, W., "Development of the Improved Helicopter Icing Spray System (IHISS)," Proceedings of the 45th Annual Forum of the American Helicopter Society, Boston, Massachusetts, May 1989.

[15]Neville, T. and Robinson, K., "Icing Trails for Qualification of the new AW101 Main and Tail Rotors, Utilising the Helicopter Icing Spray System (HISS)," Proceedings of the 66th Annual Forum of the American Helicopter Society, Phoenix, Arizona, May 2010.

[16]Lee, J. D., Harding, R., and Palko, R. L., "Documentation of ice shapes on the main rotor of a UH-1H helicopter in hover," NASA Memorandum No.168332, January 1984.

[17]Miller, T. L. and Bond, T. H., "Icing research tunnel test of a model helicopter rotor," Proceedings of the 45th Annual Forum of the American Helicopter Society, Boston, Massachusetts, May 1989.

[18]Flemming, R., Bond, T., and Britton, R., "Icing Tests of a Model Main Rotor," Proceedings of the 46th Annual Forum of the American Helicopter Society, Washington, D.C., May 1990.

[19]Tsao, J.-C. and Kreeger, R. E., "Evaluation of scaling methods for rotorcraft icing," NASA Technical Memorandum No. 215801, March 2010.

[20]Flemming, R., "The past twenty years of icing research and development at Sikorsky Aircraft," Proceedings of the 40th AIAA Aerospace Sciences Meeting & Exhibit, Reno, Nevada, January 2002.

[21]Narducci, R., Kreeger, R., "Anlaysis of a Hover Rotor in Icing Conditions," Proceedings of the 66th Annual Forum of the American Helicopter Society, Phoenix, Arizona, May 2010.

[22]Reinert, T., Flemming, R. J., Narducci, R., and Aubert, R. J., "Oscillating Airfoil Icing Tests in the NASA Glenn Research Center Icing Research Tunnel," SAE Technical Paper No. 2011-38-0016., June 2011.

[23]Fortin, G. and Perron, J., "Spinning rotor blade tests in icing wind tunnel," Proceedings of the 1st AIAA Atmospheric and Space Environments Conference, San Antonio, Texas, June 2009.

[24]Bain, J., Sankar, L. N., Aubert, R. J., and Flemming, R. J., "A methodology for the prediction of rotor blade ice formation and shedding," SAE Technical Paper No. 2011-38-0090, June 2011.

[25]Narduucci, R. and Reinert, T., "Calculations of Ice Shapes on Oscillating Airfoils," SAE Technical Paper No. 2011-38-0015, June 2011.

[26]Sears, W. R., "Some aspects of non-stationary airfoil theory and its practical application," Journal of the Aeronautical Sciences, Vol. 8 (3), January, 1941, pp. 104-108., DOI:10.2514/8.10655

[27]Carr, L. W., and McCroskey, W. J., "Analysis of the development of dynamic stall based on oscillating airfoil experiments," NASA Technical Note D-8382, January 1977.

[28]Kreeger, R. E., Sankar, L., Narducci, R., and Kunz, R., "Progress in Rotorcraft Icing Computational Tool Development," SAE Technical Paper No. 2015-01-2088, June 2015.

[29]Cheng, B., Han, Y., Brentner, K. S., Palacios, J. L., and Morris, P. J., "Quantification of rotor surface roughness due to ice accretion via broadband noise measurement," Proceedings of the 70th Annual Forum of the American Helicopter Society, Montréal, Québec, May 2014.

[30]Chen, X., Zhao, Q., and Barakos, G., "Numerical Analysis of Rotor Aero-acoustic Characteristics for Ice Detection based on HMB Solver," Proceedings of the 73rd Annual Forum of the American Helicopter Society, Fort Worth, Texas, May 2018.

[31]Zocca, M., Gori, G., and Guardone, A., "Blockage and Three-Dimensional Effects in Wind-Tunnel Testing of Ice Accretion over Wings," Journal of Aircraft, Vol. 54, (2), April 2016, pp. 759–767, DOI: https://doi.org/10.2514/1.C033750.

[32]Economon, T. D., Palacios, F., Copeland, S. R., Lukaczyk, T. W., and Alonso, J. J., "SU2: An open-source suite for multiphysics simulation and design," AIAA Journal, Vol. 54, (3), December 2015, pp. 828–846, DOI: https://doi.org/10.2514/1.J053813.

[33]Gori, G., Zocca, M., Garabelli, M., Guardone, A., and Quaranta, G., "PoliMIce: A simulation framework for three-dimensional ice accretion," Applied Mathematics and Computation, Vol. 267, September 2015, pp. 96–107, DOI: 10.1016/j.amc.2015.05.081.

[34]Gori, G., Parma, G., Zocca, M., and Guardone, A., "Local Solution to the Unsteady Stefan Problem for In-Flight Ice Accretion Modeling," Journal of Aircraft, Vol. 55, (1), September, 2017, pp. 251–262, DOI: https://doi.org/10.2514/1.C034412.

[35]Carr, L. W., McAlister, K. W., and McCroskey, W. J., "Analysis of the development of dynamic stall based on oscillating airfoil experiments," NASA Technical Note D-8382, January 1977.

[36]Zhou, B. Y., Albring, T., Gauger, N. R., Ilario, C. R., Economon, T. D., and Alonso, J. J., "Re-

duction of Airframe Noise Components Using a Discrete Adjoint Approach," Proceedings of the 18th AIAA/ISSMO Multidisciplinary Analysis and Optimization Conference, Denver, Colorado, June 2017.

[37]Richardson, L. F. and Gaunt, J. A., "VIII. The deferred approach to the limit," Philosophical Transactions of the Royal Society of London. Series A, Containing Papers of a Mathematical or Physical Character, Vol. 226, (636-646), January, 1927, pp. 299–361, DOI: https://doi.org/10.1098/rsta.1927.0008.

[38]Roache, P. J., "Perspective: a method for uniform reporting of grid refinement studies," Journal of Fluids Engineering, Vol. 116, (3), September, 1994, pp. 405–413, DOI: https://doi.org/10.1115/1.2910291.

[39]Soize, C., Ghanem, R., Safta, C., Huan, X., Vane, Z. P., Oefelein, J. C., Lacaze, G., and Najm, H. N., "Enhancing Model Predictability for a Scramjet Using Probabilistic Learning on Manifolds," AIAA Journal, Vol. 57, (1), December, 2018, pp. 365–378, DOI: https://doi.org/10.2514/1.J057069.

[40]Molina, E., Spode, C., Annes da Silva, R.G., Manosalvas-Kjono, D.E., Nimmagadda, S., Economon, T.D., Alonso, J.J. and Righi, M., "Hybrid RANS/LES calculations in SU2," Proceedings of the 23rd AIAA Computational Fluid Dynamics Conference, Denver, Colorado, June 2017.

[41]Molina E.S., Silva D.M., Broeren A.P., Righi M., Alonso J.J., Application of DDES to Iced Airfoil in Stanford University Unstructured (SU2), edited by Hoarau Y., Peng S.H., Schwamborn D., Revell A., Mockett C., Progress in Hybrid RANS-LES Modelling. Notes on Numerical Fluid Mechanics and Multidisciplinary Design, Vol. 143. Springer, Cham, November, 2019, pp 283-293, DOI: https://doi.org/10.1007/978-3-030-27607-2_23

List of Figures

List of Tables

Figures

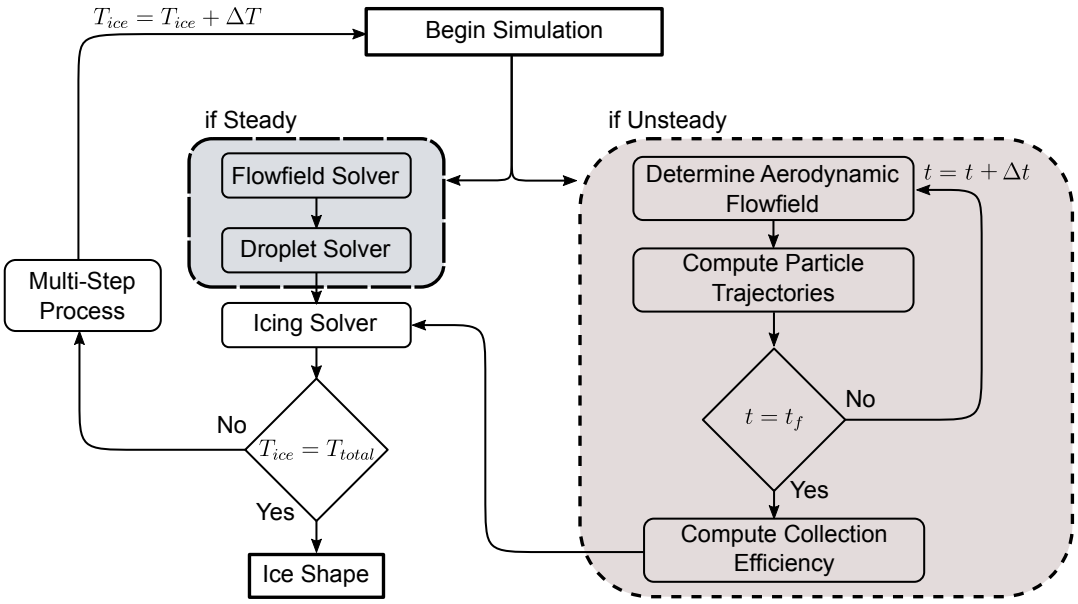

Fig. 1: Flowchart of the implementation of an ice accretion simulation. Displaying the different approaches for steady and unsteady flow field ice accretion simulations used in this work. Where, T_{ice} represents the duration of the icing simulation, and, t represents the physical time of the unsteady flow field.

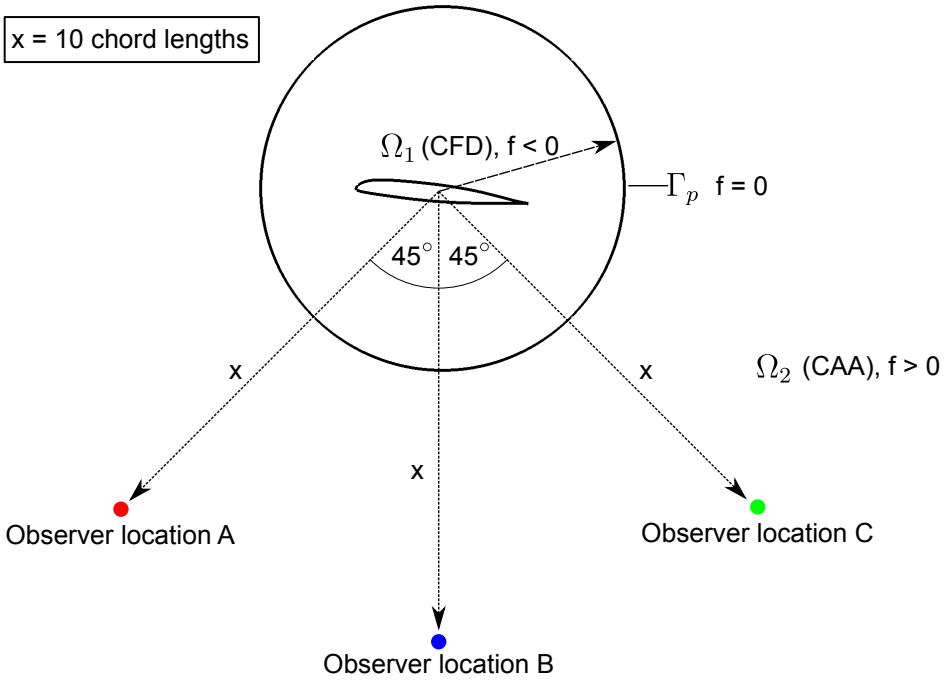

Fig. 2: Schematic of the permeable control surface Γ_p separating the CFD and CAA domains and the relative observer locations.

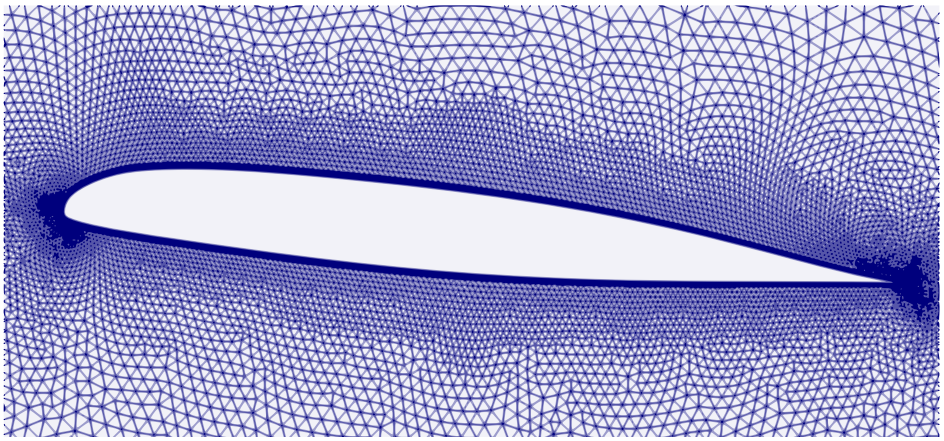

Fig. 3: Close-up of the mesh around the clean airfoil with 2-levels of surface mesh refinement.

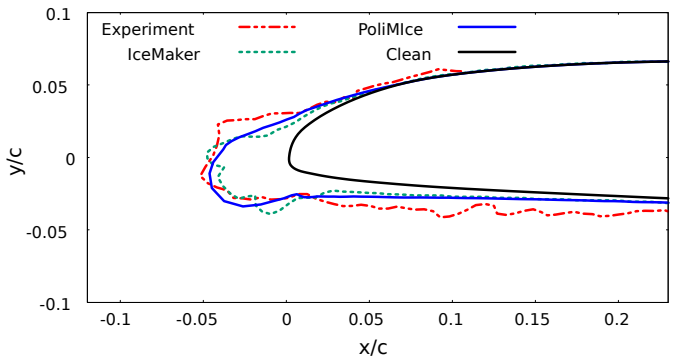

(a) Ice shapes associated to condition R-T600

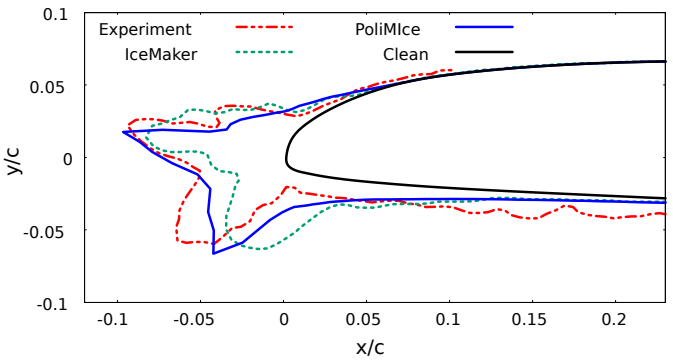

(b) Ice shapes associated to condition G-LWC

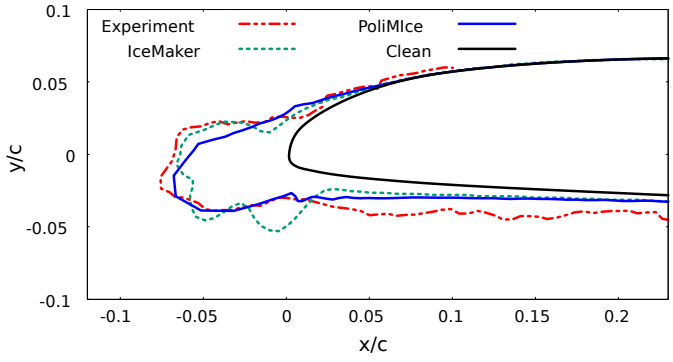

(c) Ice shapes associated to condition R-T900

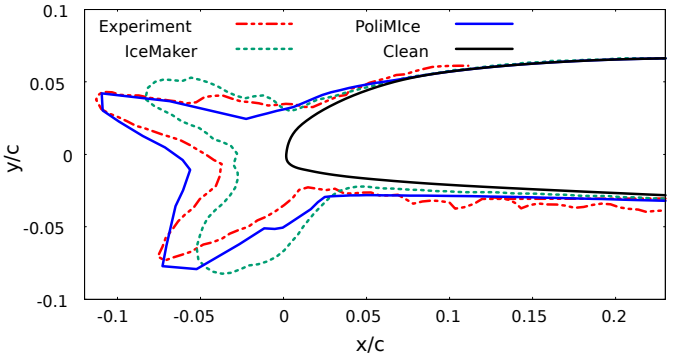

(d) Ice shapes associated to condition G-AoA5

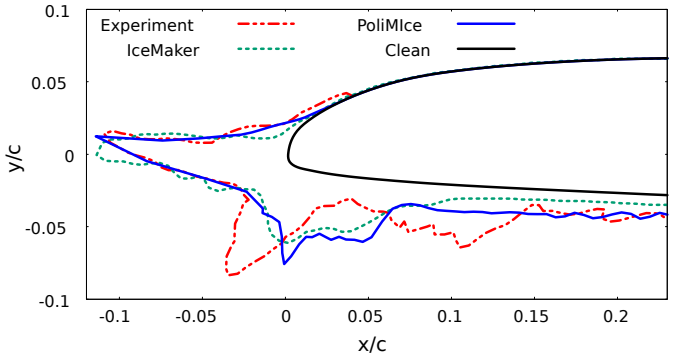

(e) Ice shapes associated to condition G-AoA10

Fig. 4: Comparison of the experimental ice shapes and simulated ice shapes from the PoliMIce and IceMaker computational icing codes. Displaying spearhead ice structures characteristic of rime ice as well as double-horn ice structures characteristic of glaze and mixed ice structures.

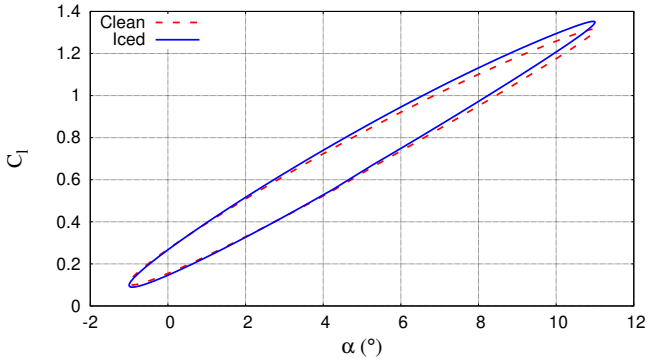

(a) Lift coefficient hysteresis loop produced from the rime ice structure of R-T600.

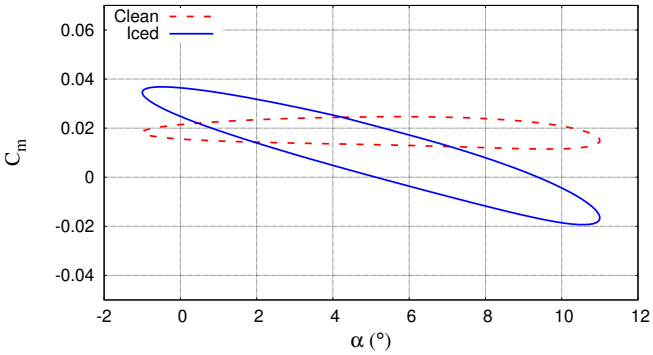

(b) Moment coefficient hysteresis loop produced from the rime ice structure of R-T600.

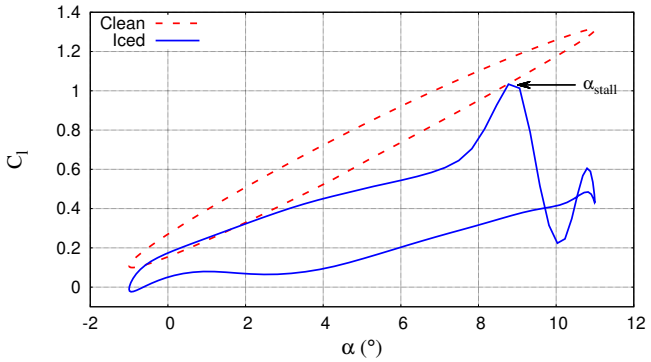

(c) Lift coefficient hysteresis loop produced from the glaze ice structure of G-LWC.

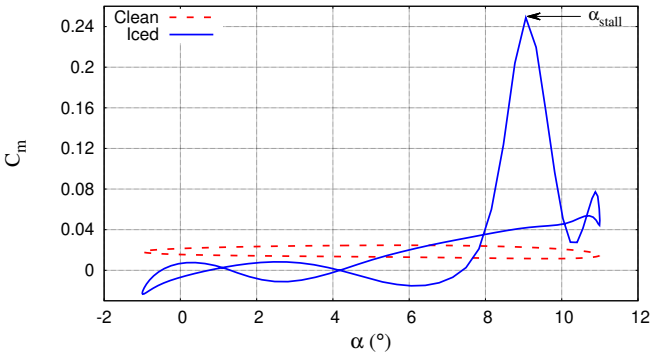

(d) Moment coefficient hysteresis loop produced from the glaze ice structure of G-LWC.

Fig. 5: Comparison of the predicted clean and iced airfoil lift and moment coefficients hysteresis loops generated from conditions R-T600 and G-LWC based on the test matrix from Table 1. Displaying the detrimental influence the double-horn ice structure generated during glaze conditions has on the airfoils dynamic performance.

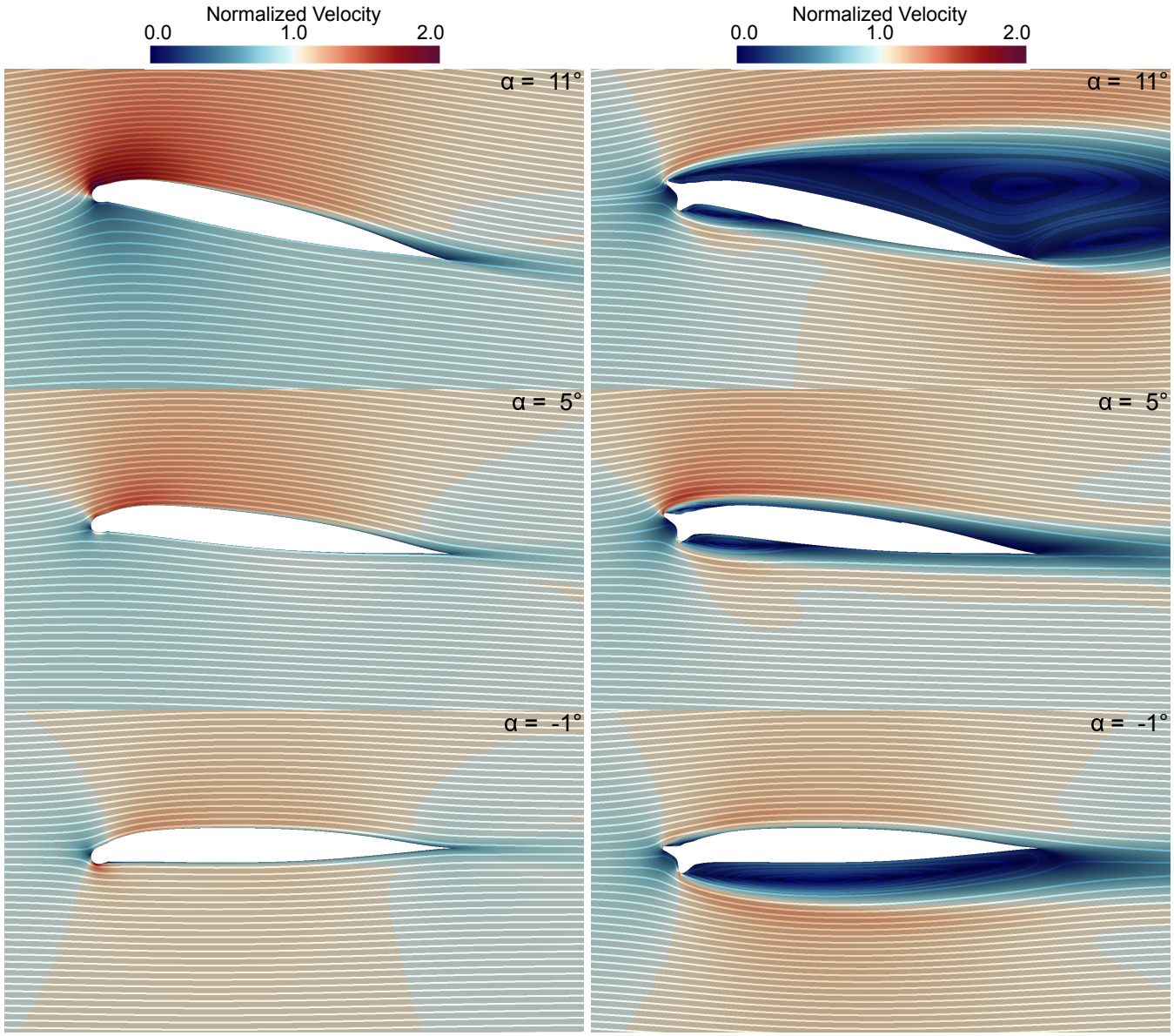

(a) Flow field produced from the rime ice structure during condition R-T600.

(b) Flow field produced from the glaze ice structure during condition G-LWC.

Fig. 6: Flow field comparison of glaze and rime iced airfoils from Table 1. Diagram shows the normalized velocity flow field and uniformly spaced streamlines across the flow fields. Where the velocity is normalized by the incoming free-steam velocity.

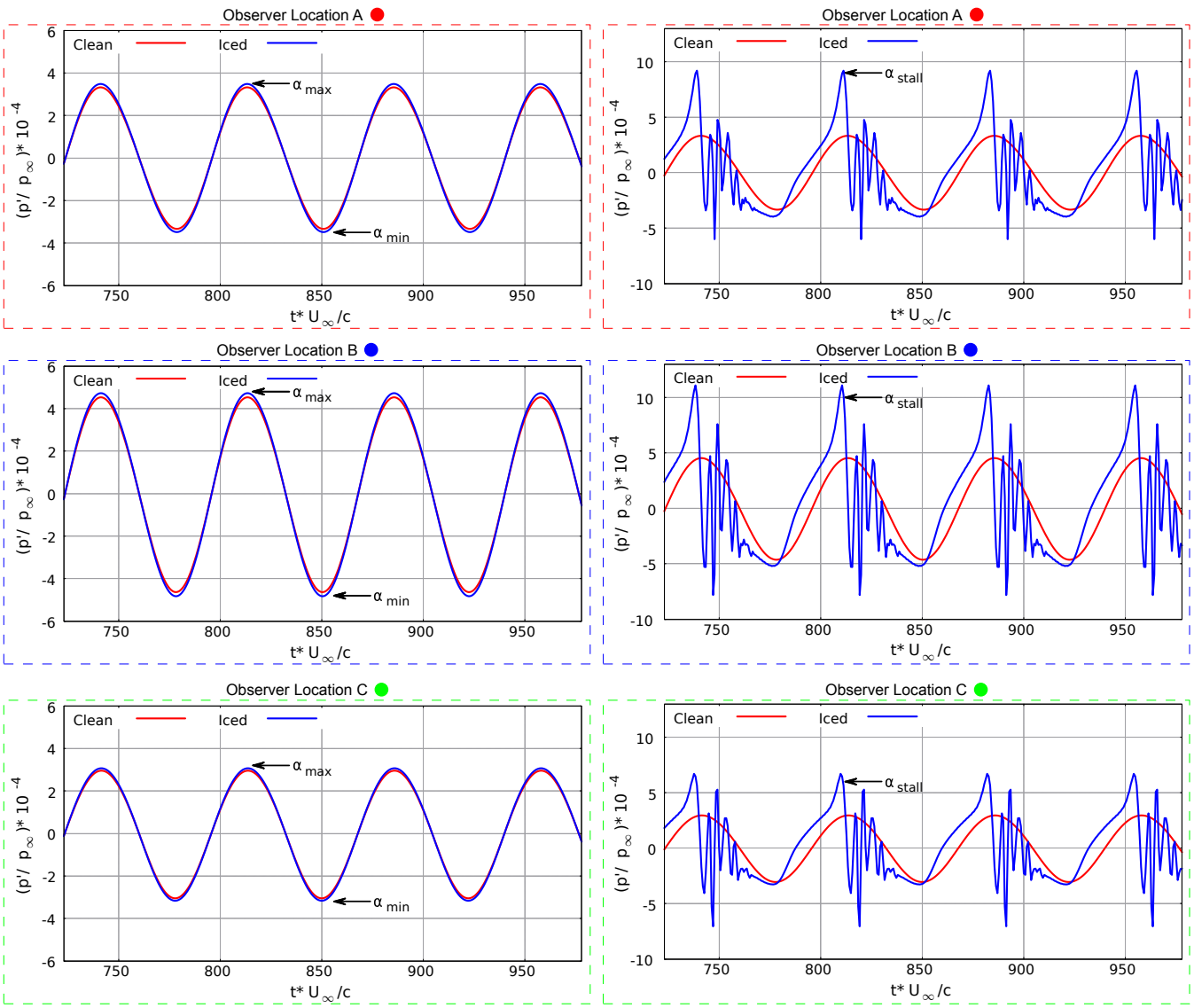

(a) Acoustic signal produced from the rime ice structure during condition R-T600.

(b) Acoustic signal produced from the glaze ice structure during condition G-LWC.

Fig. 7: Comparison of the predicted clean and iced airfoil acoustic signals from Table 1. Displays the acoustic signals over a time window long enough to display their periodicity related to the oscillation of the airfoil. Where the acoustic pressure is normalized by freestream pressure and the time is non-dimensionalized to the convective time unit based on the freestream velocity and the chord length.

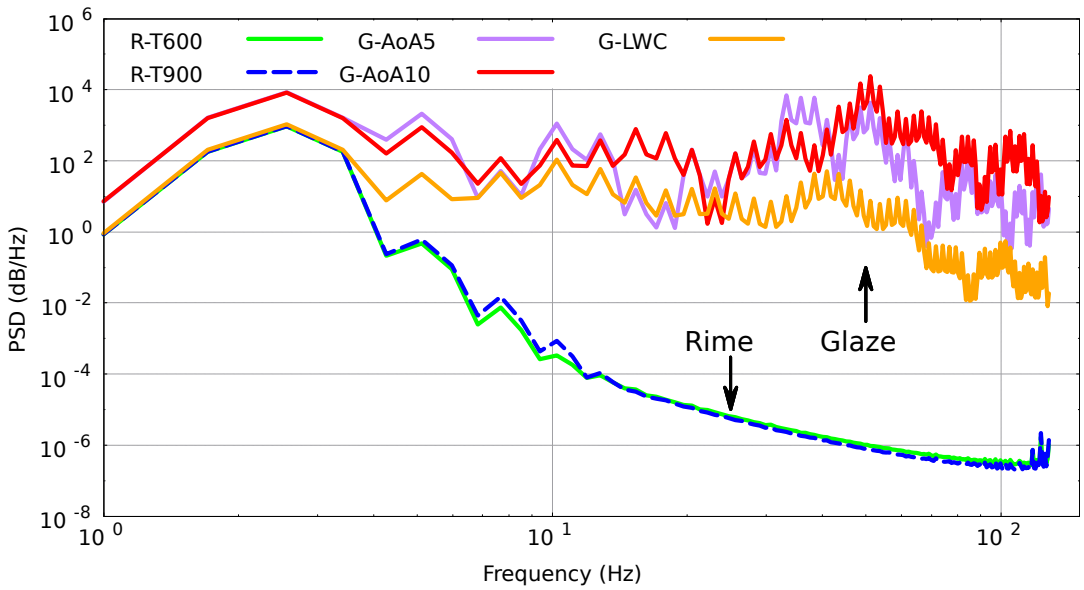

Fig. 8: Far-field sound spectra of the iced airfoils. Displaying how the sound spectra can be characterized into two distinct noise signals produced from glaze and rime ice structures. R-T600 and R-T900 represent the test conditions where rime ice was formed and G-LWC, G-AoA5 and G-AoA10 represent the test conditions where glaze ice was formed.

Tables

Table 1: Test cases chosen for examination taken from Rienert et al.[α]. Conditions selected to produce a range of ice shapes and assess multiple influential parameters in both glaze and rime ice regimes.

Test Case [-]	Air Speed $[m/s]$	Oscillation Frequency $[Hz]$	Oscillating Motion [°]	LWC $[g/m^3]$	Time $[seconds]$	Ice Type [-]
R-T600	77	2.8	5 ± 6	0.5	600	Rime
G-LWC	77	2.8	5 ± 6	1.0	600	Glaze
R-T900	77	2.8	5 ± 6	0.5	900	Rime
G-AoA5	135	2.8	5 ± 6	0.5	600	Glaze
G-AoA10	135	2.8	10 ± 6	0.5	600	Glaze

[α]Test cases based on the experimental work from Rienert et al. in the NASA IRT facilities Ref. 22

Table 2: Mesh refinement levels

Refinement Level [-]	Surface Node Spacing $[m]$	Refinement Ratio [-]	y^+ [-]	C_l [-]	C_d [-]
1	0.00100	2	0.77	0.728955	0.011112
2	0.00050	2	0.77	0.725284	0.011036
3	0.00025	2	0.77	0.724400	0.011018

Table 3: Grid Convergence Index results

f	ε_{32}	ε_{21}	p	f_{exact}	GCI_{32}	GCI_{21}
C_l	1.22	5.04	1.94	0.724090	0.53%	2.21%
C_d	1.63	6.84	1.92	0.011011	0.73%	3.07%